Multifunctional Molecule-Grafted V$_2$C MXene as High-Kinetics Potassium-Ion-Intercalation Anodes for Dual-Ion Energy Storage Devices

Davood Sabaghi, Josef Polčák, Hyejung Yang, Xiaodong Li, Ahiud Morag, Dongqi Li, Ali Shaygan Nia, Saman Khosravi H, Tomáš Šikola, Xinliang Feng,* and Minghao Yu*

Constructing dual-ion energy storage devices using anion-intercalation graphite cathodes offers the unique opportunity to simultaneously achieve high energy density and output power density. However, a critical challenge remains in the lack of proper anodes that match with graphite cathodes, particularly in sustainable electrolyte systems using abundant potassium. Here, a surface grafting approach utilizing multifunctional azobenzene sulfonic acid is reported, which transforms V$_2$C MXene into a high-kinetics K$^+$-intercalation anode (denoted ASA-V$_2$C) for dual-ion energy storage devices. Importantly, the grafted azobenzene sulfonic acid offers extra K$^+$-storage centers and fast K$^+$-hopping sites, while concurrently acting as a buffer between V$_2$C layers to mitigate the structural distortion during K$^+$ intercalation/de-intercalation. These functionalities enable the V$_2$C electrode with significantly enhanced specific capacity (173.9 mAh g^{-1} vs 121.5 mAh g^{-1} at 0.05 A g^{-1}), rate capability (43.1% vs 12.0% at 20 A g^{-1}), and cycling stability (80.3% vs 45.2% after 900 cycles at 0.05 A g^{-1}). When coupled with an anion-intercalation graphite cathode, the ASA-V$_2$C anode demonstrates its potential in a dual-ion energy storage device. Notably, the device depicts a maximum energy density of 175 Wh kg^{-1} and a supercapacitor-comparable power density of 6.5 kW kg^{-1}, outperforming recently reported Li$^+$-, Na$^+$-, and K$^+$-based dual-ion devices.

1. Introduction

Driven by the increasing energy demand spanning from individual electronics to grid storage applications, electrochemical energy storage devices have become a vibrant area of focus for both academic research and practical applications.[1,2] Supercapacitors and batteries possess nearly opposite power and energy characteristics due to their distinct electrochemical mechanisms.[3] However, the need for both power and energy density are equally crucial for real-world energy storage applications and is expected to continually grow. Consequently, it is strongly desired to develop advanced energy storage devices that can mitigate the power-energy tradeoff.[4–6] One approach to tackle this dilemma is to adopt high-kinetics ion-intercalation anodes/cathodes to assemble full devices. Such electrodes involve Faradaic redox reactions of the bulk electrode with large charge-storage

D. Sabaghi, H. Yang, A. Morag, D. Li, A. S. Nia, S. Khosravi H, X. Feng, M. Yu
Department of Chemistry and Food & Center for Advancing Electronics Dresden (cfaed)
Technische Universität Dresden
01062 Dresden, Germany
E-mail: xinliang.feng@tu-dresden.de; minghao.yu@tu-dresden.de

J. Polčák, T. Šikola
CEITEC-Central European Institute of Technology
Brno University of Technology
Purkynova 123, Brno 61200, Czech Republic

J. Polčák, T. Šikola
Faculty of Mechanical Engineering
Institute of Physical Engineering
Brno University of Technology
Technicka 2896/2, Brno 61669, Czech Republic

X. Li, A. Morag, A. S. Nia, X. Feng
Max Planck Institute of Microstructure Physics
D-06120 Halle (Saale), Germany

capacity, while allowing high rate performance with superior fast-charging capability.[2,7] A representative cathode that fulfills these criteria is graphite with favorable anion-intercalation chemistries (such as hexafluorophosphate, bis(fluorosulfonyl)imide, and bis(trifluoromethanesulfonyl)imide anions).[8] The graphite cathode can deliver a large specific capacity of up to 100 mAh g^{-1}, a high average discharge potential of >1.5 V versus standard hydrogen electrode, and ultrafast rate capability (up to 100 C).[9] A variety of dual-ion energy storage devices using typical Li-ion battery electrolytes have been demonstrated by pairing graphite cathode with different Li^+-hosting anode materials, such as graphite,[10] WS_2,[11] α-MoO_3,[12] and $TiSe_2$.[13] Beyond Li systems, extending the dual-ion device concept to more sustainable systems using abundant elements like K is even more attractive, which, however, has been seldom explored.[14–16] The challenge in utilizing K^+ arises from its considerably larger size (1.38 Å in radius) compared with Li^+ (0.76 Å in radius). This size difference poses a critical challenge in finding suitable K^+-hosting anode materials that can concurrently match with the specific capacity and rate capability of anion-intercalation graphite.[17]

MXenes, which can be represented by the formula $M_{n+1}X_nT_x$ ($n = 1 – 4$, M is a transition metal, X is N and/or C, and T_x is terminal groups), have gained considerable attention as a versatile group of 2D transition metal carbide and/or nitride materials.[18–21] Particularly, their slit-shaped 2D nanochannels and metallic nature with high electrical conductivity allow MXenes to exhibit favorable cation intercalation and hosting capability as pseudocapacitive anode materials.[22] As a representative example, Ti_3C_2 MXene showed a decent Li^+-hosting capacity of 468 C g^{-1} (130 mAh g^{-1}) and excellent rate performance with capacity retention of 61% from 2 to 1000 mV s^{-1} in a non-aqueous lithium bis(trifluoromethanesulfonyl)imide electrolyte.[23] Moreover, early studies have widely demonstrated that the Li^+-hosting capacity of MXenes could be considerably boosted by modifying their layered structures in terms of surface chemistry[24–26] and interlayer space.[27–29] Compared with Li^+-hosting MXenes, progress in K^+-hosting MXenes appears to be much retarded. Apparently, the large size of K^+ leads to problematic K^+-intercalation kinetics in MXenes, limiting their charge-storage capacity and rate capability.[30–32,33,34] For instance, pristine V_2C anode [33] and Ti_3CN anode[30] at 0.05 A g^{-1} were shown to exhibit limited specific capacities of 98 mAh g^{-1} and 65 mAh g^{-1}, respectively. Although the K^+-storage capability of Ti_3C_2 MXene was boosted by the alkalization treatment, the obtained Ti_3C_2 nanoribbons only depicted a specific capacity of 78 mAh g^{-1} at 0.2 A g^{-1}.[34] Moreover, Wang et al.[35] pioneered the construction of 3D $Ti_3C_2T_x$ MXene porous frameworks using electrostatic flocculation and subsequent K^+-preintercalation. Compared with conventional 2D $Ti_3C_2T_x$, the obtained 3D $Ti_3C_2T_x$ showed an apparent enhancement in the K^+-storage capability, which was assigned to the unique aggregation-resistant structure and enlarged interlayer distance. Clearly, developing efficient approaches to promote K^+-intercalation kinetics of MXenes would be highly desirable, as it opens up opportunities to obtain fast-charging anodes that can be coupled with anion-intercalation graphite to assemble high-performance dual-ion energy storage devices.

Herein, we present the grafting of multifunctional azobenzene sulfonic acid on V_2C MXene (denoted ASA-V_2C) as an effective strategy to yield high-kinetics K^+-intercalation anodes, which fur-

ther enables the assembly of dual-ion energy storage devices characterized by both high energy and power densities. The grafting of azobenzene sulfonic acid is achieved through the amine diazotization and subsequent diazonium removal reaction of 4-aminoazobenzene-4′-sulfonic acid sodium salt, resulting in the apparent expansion of the interlayer distance from 0.86 nm for pristine V_2C to 1.25 nm for ASA-V_2C. We demonstrate the significantly enhanced specific capacity (173.9 mAh g^{-1} vs 121.5 mAh g^{-1} at 0.05 A g^{-1}) and rate capability (43.1% vs 12.0% at 20 A g^{-1}) of the ASA-V_2C electrode in comparison with the V_2C electrode. This enhancement can be attributed to the presence of azobenzene units that offer extra K^+-storage centers, along with sulfonate anions serving as rapid K^+-hopping sites. Moreover, the grafted "soft" molecules not only expand the interlayer distance of V_2C but also act as an internal strain buffer during repeated K^+ intercalation/de-intercalation, which effectively alleviates structural distortion and improves the long-term cycling stability of the ASA-V_2C electrode (80.3% vs 45.2% after 900 cycles at 0.05 A g^{-1}). Furthermore, we demonstrate a dual-ion energy storage device with an operation voltage window of 2.5 – 4.5 V by coupling our ASA-V_2C anode with an anion-intercalation graphite cathode. By capitalizing on the high-kinetics ion intercalation/de-intercalation processes at both the anode and cathode, the assembled device delivers a maximum energy density of 175 Wh kg^{-1} and a power density comparable to supercapacitors (6.5 kW kg^{-1} at 65 Wh kg^{-1}), significantly surpassing recently reported Li^+-, Na^+-, and K^+-based dual-ion devices.

2. Results and Discussion

2.1. Synthesis and Characterization of ASA-V_2C

V_2C was chosen for our investigation due to its superior chemical stability compared to other M_2X-type MXenes (e.g., Ti_2C and Nb_2C) and classic Ti_3C_2 MXenes, as suggested by the recent theoretical prediction.[36] Our electrochemical measurements also revealed the higher K^+-storage capacities of V_2C than those of Ti_2C, Nb_2C, and Ti_3C_2 (Figure S1, Supporting Information). The covalent grafting of multifunctional azobenzene sulfonic acid onto V_2C was achieved using 4-aminoazobenzene-4′-sulfonic acid sodium salt as the starting molecule (**Figure 1a**), involving amine diazotization and subsequent diazonium removal reactions (Figure 1b). Specifically, the amino group of 4-aminoazobenzene-4′-sulfonic acid sodium salt was first converted to a diazonium salt (-$N_2^+Cl^-$) by reacting with $NaNO_2$ and HCl in an iced bath.[37] At the same time, sulfonic acid sodium salt underwent conversion into sulfonic acid in the strong acidic environment. The V_2C dispersion was next added to the yielded diazonium salt solution in an iced bath. Along with the temperature reached room temperature, the diazonium group dissociated from the molecule, generating radical compounds that subsequently bonded with electronegative surface terminals of V_2C MXene (such as -O and -F groups). The grafted organic molecule was expected to confer multiple benefits to the K^+-storage performance of V_2C. 1) The azobenzene unit exhibits a favorable redox-active nature, enabling the extra K^+-storage site (Figure 1c). 2) The sulfonate anion would act as the desirable K^+-hopping site, accelerating interlayer K^+ diffusion (Figure 1d). 3) The soft organic molecules between V_2C layers could efficiently widen the
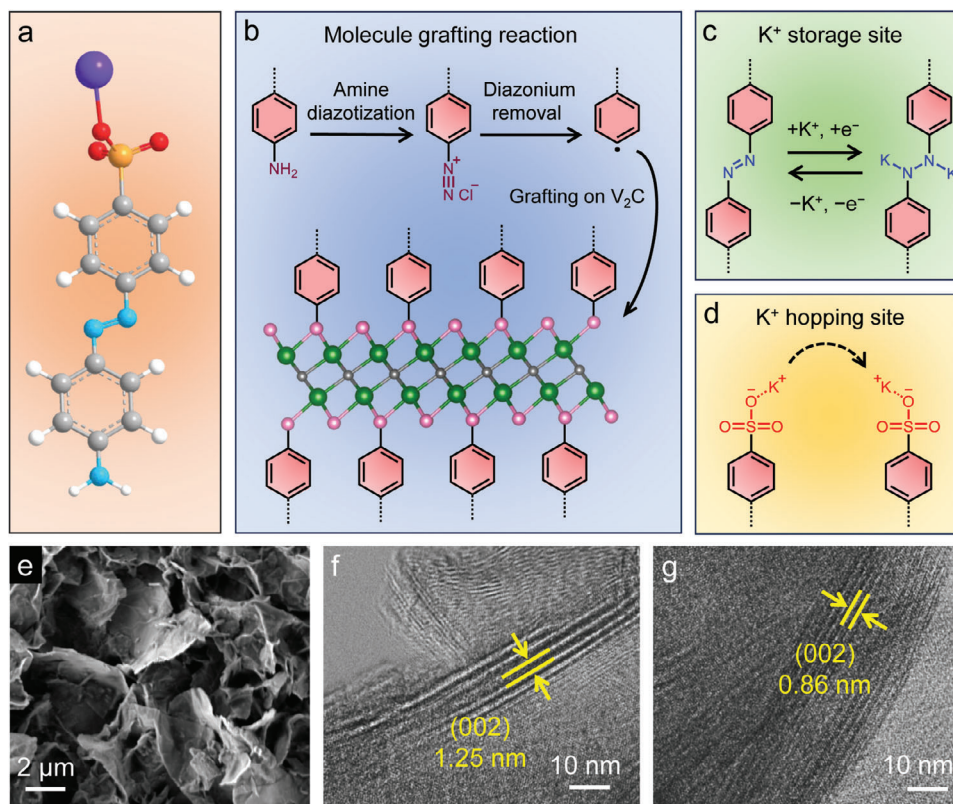
Figure 1. Schematic illustration showing a) 4-aminoazobenzene-4′-sulfonic acid sodium salt (white sphere: H; grey sphere: C; blue sphere: N; orange sphere: S; red sphere: O; purple sphere: Na), b) molecule grafting reaction (black sphere: C; green sphere: V; pink sphere: the terminals of V_2C MXene), c) the azobenzene unit as the extra K^+-storage site, and d) the sulfonate anion as the K^+-hopping site. e) Scanning electron microscopy image of ASA-V_2C nanoflakes. HR-TEM images of f) the ASA-V_2C film and g) the pristine V_2C film.

interlayer gap and buffer the internal stress arising from repeated K^+ intercalation/de-intercalation.

In contrast to the planar nanoflakes of pristine V_2C (Figure S2, Supporting Information), the obtained ASA-V_2C nanoflakes display a noticeably curved morphology (Figure 1e). This curvature is expected to mitigate the common re-stacking issue of 2D materials and enable efficient ion transport channels among the nanoflakes. ASA-V_2C nanoflakes were subsequently vacuum-filtered to form a free-standing film with a thickness of 36 μm (Figure S3, Supporting Information). High-resolution transmission electron microscopy (HR-TEM) was used to evaluate the cross-sectional structure of the ASA-V_2C film (Figure 1f), revealing an interlayer distance of 1.25 nm. This value represents a significant expansion compared to 0.86 nm for the pristine V_2C film (Figure 1g).

For comparison, we also grafted biphenyl onto V_2C (denoted BP-V_2C) with benzidine as the starting molecule, employing similar amine diazotization and diazonium removal reactions (Figure S4, Supporting Information). Unlike the grafted azobenzene sulfonic acid, biphenyl is not equipped with redox-active unit and favorable cation-hopping site. The thermogravimetric analysis detected the stable grafting of organic molecules until a high temperature of 259 °C (**Figure 2a**). It is estimated that the organic molecule accounts for 8.3% and 9.1% of the total weight of BP-V_2C and ASA-V_2C, respectively. Fourier transform infrared (FTIR) spectra further confirmed the successful grafting of or-

ganic molecules (Figure 2b). Characteristic peaks of phenyl units, including aromatic C = C stretching (1474 cm^{-1}) and aromatic C-H in-plane bending (1010 and 1086 cm^{-1}),[38] were clearly observed for both BP-V_2C and ASA-V_2C. The peak of ASA-V_2C at 1119 cm^{-1} verifies the presence of sulfonic acid group (-SO_3H stretching),[38] while its N = N stretching(1474 cm^{-1}) overlaps with aromatic C = C stretching.

X-ray photoelectron spectroscopy (XPS) was further conducted on the three samples to evaluate the oxidation of V_2C. In the V 2p XPS spectrum of pristine V_2C (Figure 2c), four deconvoluted peaks can be detected, corresponding to V $2p_{1/2}$ peaks of V^{4+} (523.8 eV) and V^{2+}/V-C (520.9 eV), as well as V $2p_{3/2}$ peaks of V^{4+} (516.3 eV) and V^{2+}/V-C (513.4 eV).[39] The presence of high-valence V^{4+} indicates surface oxidation of V_2C. In comparison with V_2C, ASA-V_2C shows a much weaker V 2p XPS signal (Figure 2d), while the signal is even marginal for BP-V_2C (Figure 2e). This observation suggests dense and homogeneous coverage of functional molecules on the V_2C surface. Following 20 keV Ar$^+$ cluster sputtering for 5 min, the V 2p signal intensity of BP-V_2C and ASA-V_2C become substantially enhanced. Both BP-V_2C and ASA-V_2C show dominant V^{2+}/V-C peaks, and their high-valence V^{4+} peaks are considerably suppressed. This result reflects the effective role of the grafted molecules in inhibiting surface oxidation of V_2C. During the functionalization process, the diazonium salt tends to take the lone pair electron from surface -O/-OH terminals of MXene, leading to the grafting
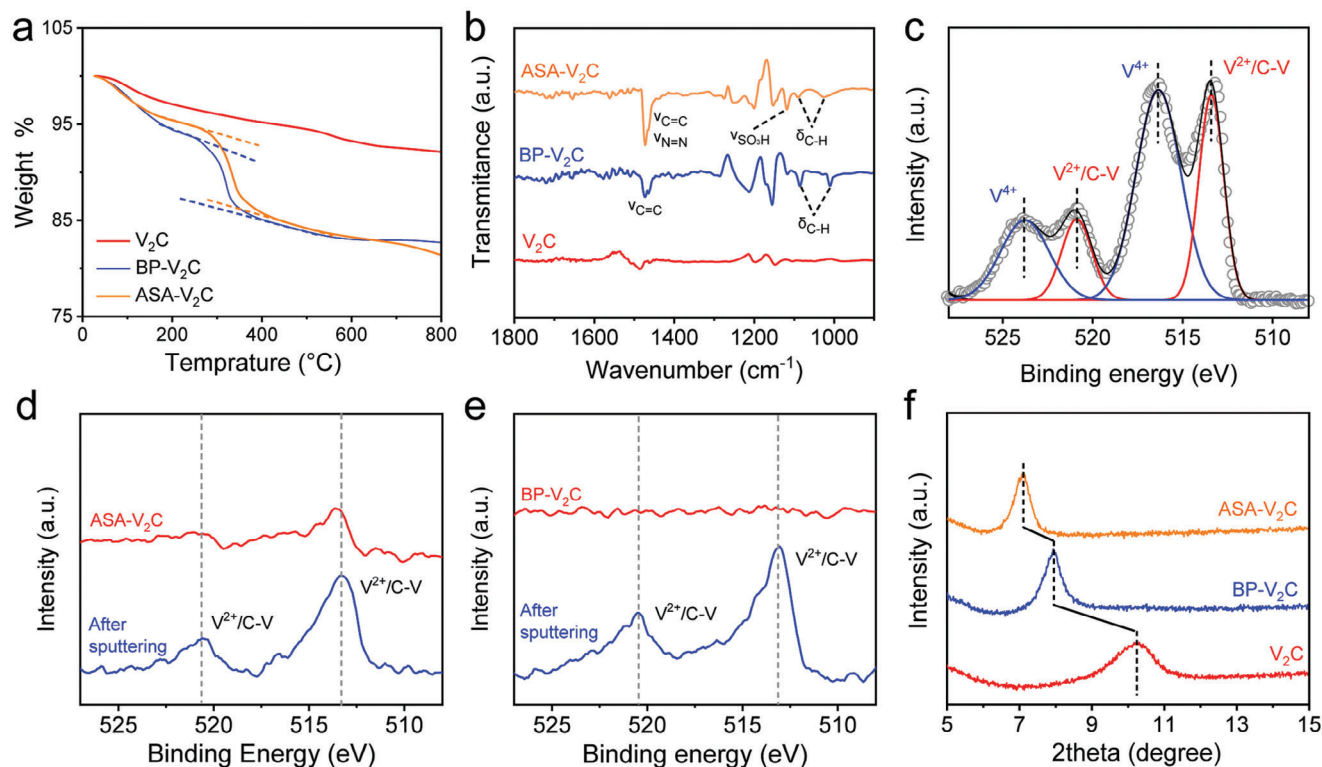
ADVANCED
SCIENCE NEWS

www.advancedsciencenews.com

ADVANCED
ENERGY
MATERIALS

www.advenergymat.de

Figure 2. a) Thermogravimetric analysis and b) FTIR spectra of V$_2$C, BP-V$_2$C, and ASA-V$_2$C. V 2p XPS spectra of c) V$_2$C, d) BP-V$_2$C, and e) ASA-V$_2$C. f) XRD patterns of V$_2$C, BP-V$_2$C, and ASA-V$_2$C.

of molecules via the formation of metal-O-C bonds. This process is evidenced by the O1s XPS result of ASA-V$_2$C (Figure S5, Supporting Information), which reveals the presence of the V-O-C peak at 529.3 eV.[40,41]

Furthermore, Figure 2f compares the X-ray diffraction (XRD) patterns of pristine V$_2$C, BP-V$_2$C, and ASA-V$_2$C. The characteristic (002) peak undergoes a clear negative shift from V$_2$C (10.3°) to BP-V$_2$C (7.9°) and ASA-V$_2$C (7.1°), indicating the gradual expansion of the interlayer distance. Based on Bragg's Law, d-spacings were determined to be 0.86, 1.12, and 1.25 nm for V$_2$C, BP-V$_2$C, and ASA-V$_2$C, respectively. These results are in good agreement with the measured interlayer distance in HR-TEM images.

2.2. Performance of ASA-V$_2$C as the K$^+$-Storage Anode

The K$^+$-storage performance of free-standing V$_2$C, BP-V$_2$C, and ASA-V$_2$C films was evaluated in two-electrode Swagelok cells with an electrolyte of 5 M potassium bis(fluorosulfonyl)imide (KFSI) dissolved in a mixture of dimethyl carbonate and ethylene carbonate (1:1 vol.%). **Figure 3a** compares the cyclic voltammetry (CV) curves of the three electrodes at 0.5 mV s^{-1}. Apparently, ASA-V$_2$C presents the largest CV area among the three electrodes, indicating its superior K$^+$-storage capacity. Its charge storage capability is shown dominantly below 1.5 V versus K$^+$/K. The CV curve shows a quasi-rectangular shape below 1.5 V versus K$^+$/K, reflecting the pseudocapacitive K$^+$-intercalation characteristics of ASA-V$_2$C. The extra K$^+$-storage centers contributed by the grafted azo-compound are evidenced by the presence of

pronounced redox peaks at 0.6 – 1.5 V versus K$^+$/K,[42] which are consistent with the CV curve of the starting molecule, 4-aminoazobenzene-4′-sulfonic acid sodium salt (Figure S6, Supporting Information). In addition, a pair of broad redox peaks can be observed for ASA-V$_2$C at 2.0 – 2.5 V versus K$^+$/K, and they can be assigned to the presence of vanadium oxides clusters due to the inevitable oxidation of V$_2$C during material preparation.[43]

To assess the rate capability of the three electrodes, galvanostatic charge/discharge (GCD) curves were collected at various current densities ranging from 0.05 to 20 A g^{-1} (Figure 3b; Figure S7, Supporting Information). As depicted in Figure 3c, the ASA-V$_2$C electrode exhibits a remarkable specific capacity of 173.9 mAh g^{-1} at 0.05 A g^{-1}, greatly surpassing the specific capacities of the V$_2$C electrode (121.5 mAh g^{-1}) and the BP-V$_2$C electrode (136.9 mAh g^{-1}). Of significant note, at a significantly increased current density of 20 A g^{-1} (referring to a short charge/discharge time of ≈13.5 s)‚ the ASA-V$_2$C electrode maintains a decent specific capacity of 74.9 mAh g^{-1}, equivalent to 43.1% of its maximum specific capacity. In contrast, the V$_2$C electrode and the BP-V$_2$C electrode at 20 A g^{-1} only exhibit capacity retention of 12.0% and 17.4%, respectively. Specific capacities as a function of charge/discharge time were further plotted for the ASA-V$_2$C electrode (Figure 3d), highlighting the state-of-the-art performance in comparison with recently reported K$^+$-storage MXene anodes, such as V$_2$C,[33] Ti$_3$CN,[30] alkalized Ti$_3$C$_2$,[34] and Ti$_3$C$_2$ nanoribbons.[44] We further collected CV curves of V$_2$C, BP-V$_2$C, and ASA-V$_2$C at varying scan rates. Using Equation (1) with i as the current and v as the scan rate, the CV curves are separated into the capacitive-controlled section (k_1v) and the
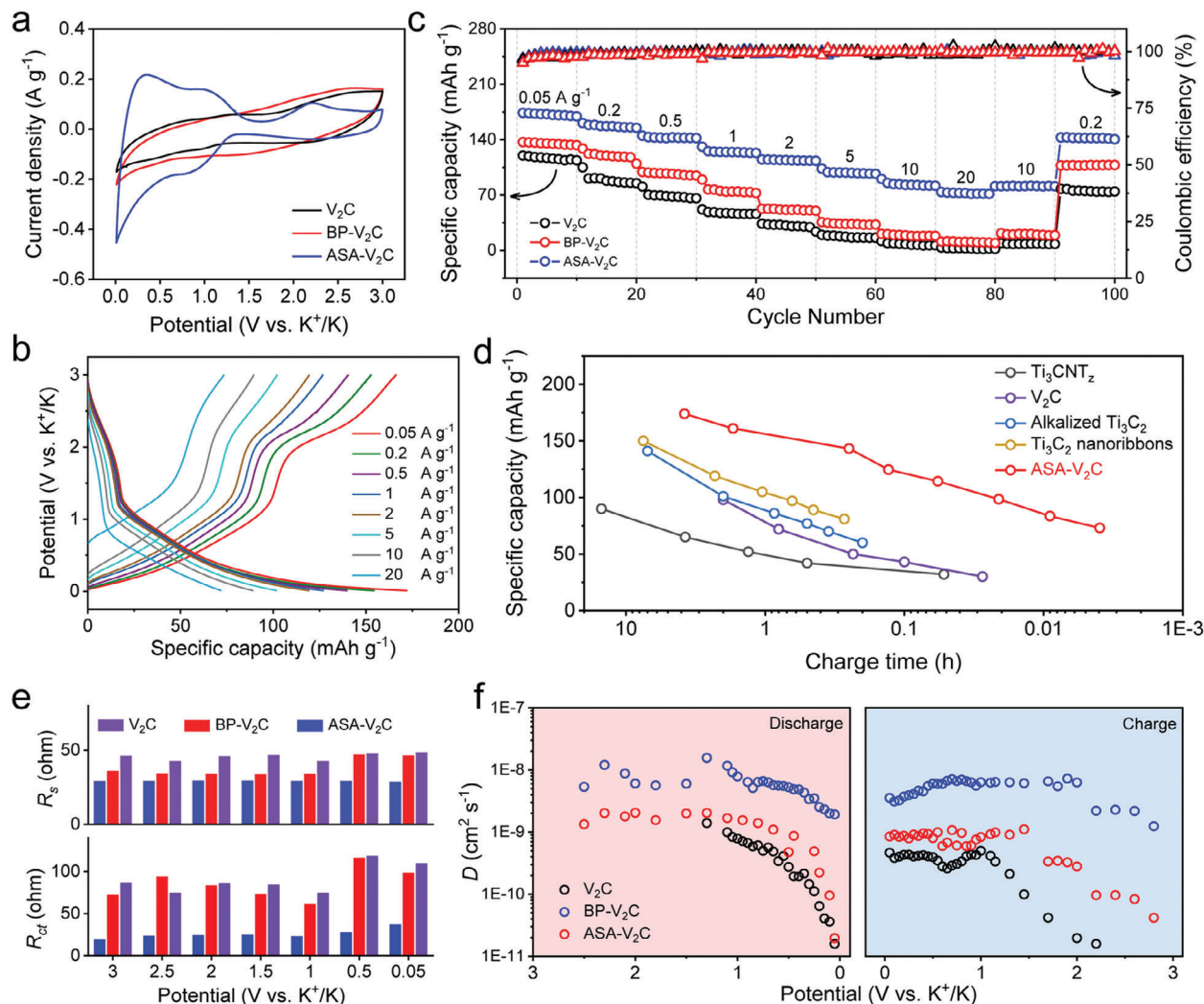
2302961 (4 of 9)

ADVANCED
SCIENCE NEWS

www.advancedsciencenews.com

ADVANCED
ENERGY
MATERIALS

www.advenergymat.de

Figure 3. a) CV curves at 0.5 mV s^{-1} and b) rate performance of the V$_2$C, BP-V$_2$C, and ASA-V$_2$C electrodes. c) GCD profiles of the ASA-V$_2$C electrode at various current densities. d) Specific capacity as a function of charge time for the ASA-V$_2$C electrode in comparison with recently reported K$^+$-intercalation MXene electrodes. e) R_s and R_{ct} of the V$_2$C, BP-V$_2$C, and ASA-V$_2$C electrodes derived from the EIS measurements. f) K$^+$ diffusion coefficients of the V$_2$C, BP-V$_2$C, and ASA-V$_2$C electrodes calculated from the GITT measurements.

diffusion-controlled section ($k_2 v^{1/2}$). As shown in Figure S8 (Supporting Information), ASA-V$_2$C presents the largest capacitive contribution among the three electrodes across all scan rates. This analysis highlights the obviously enhanced K$^+$ intercalation kinetics.

$$i = k_1 v + k_2 v^{1/2} \qquad (1)$$

Electrochemical impedance spectroscopy (EIS) was performed on the three electrodes at various potentials to gain insights into the performance improvement induced by the grafted molecules (Figure S9, Supporting Information). The values of Ohmic resistance (R_s) and charge transfer resistance (R_{ct}) for the three electrodes (Figure 3d) were derived by fitting the EIS data with an equivalent circuit shown in Figure S9 (Supporting Information). Across all potentials, R_s follows the trend of V$_2$C > BP-V$_2$C > ASA-V$_2$C, suggesting that the grafted molecule effectively

enhance the charge transport capability of V$_2$C. Moreover, the significantly improved charge transfer of ASA-V$_2$C was evident from its pronouncedly lower R_{ct} (38.0 Ω at 0.05 V vs K$^+$/K) in comparison with V$_2$C (110.8 Ω at 0.05 V vs K$^+$/K) and BP-V$_2$C (99.6 Ω at 0.05 V vs K$^+$/K). In addition, K$^+$ diffusion coefficient (D) within the three electrode was quantified using the galvanostatic intermittent titration technique (GITT, Figure S10, Supporting Information). As expected, ASA-V$_2$C demonstrates the fastest K$^+$ diffusion with D values of $1.2 \times 10^{-9} - 1.6 \times 10^{-8}$ cm^2 s^{-1}, significantly outclassing V$_2$C ($1.6 \times 10^{-11} - 1.4 \times 10^{-9}$ cm^2 s^{-1}) and BP-V$_2$C ($2.0 \times 10^{-11} - 2.0 \times 10^{-9}$ cm^2 s^{-1}). All these results underscore the significant role of sulfonate anions equipped on the grafted molecules in accelerating K$^+$ diffusion between V$_2$C layers.

In addition to the boosted K$^+$-storage kinetics, the grafted molecule also significantly enhanced the cycling stability of V$_2$C (**Figure 4a**). During the long-term cycle test at a low current
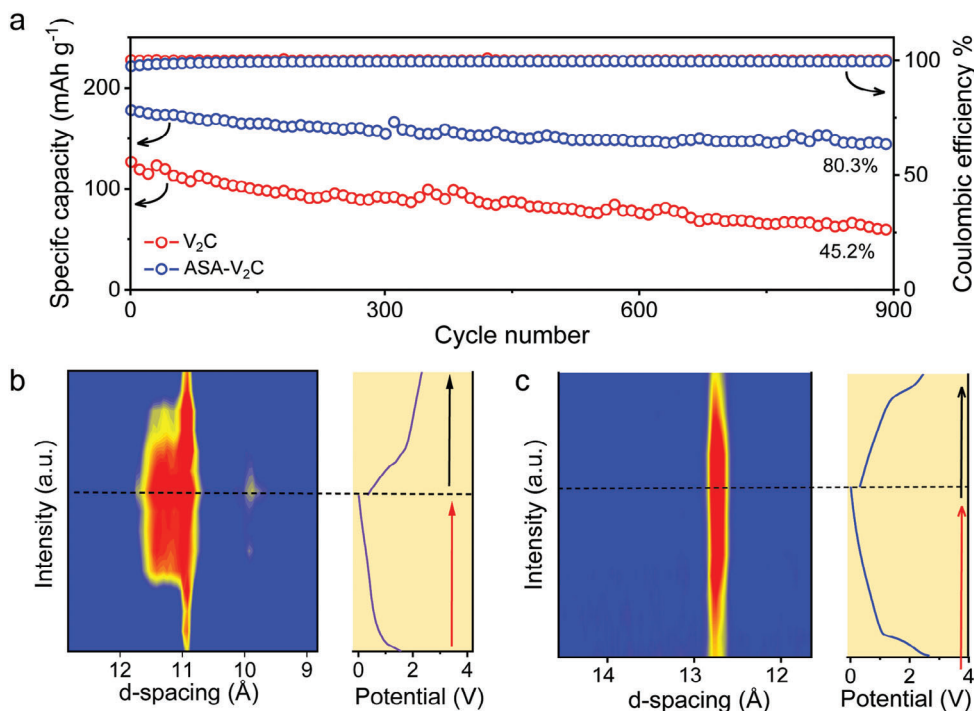
2302961 (5 of 9)

Figure 4. a) Cycling performance of the V_2C, and ASA-V_2C electrodes at 0.05 A g^{-1}. Synchrotron operando XRD spectra of the b) V_2C and c) ASA-V_2C electrodes during one charge/discharge cycle.

density of 0.05 A g^{-1}, the specific capacity of the V_2C electrode experienced a noticeable decay, reducing to only 45.2% of its initial specific capacity after 900 charge/discharge cycles. Contrastingly, the ASA-V_2C electrode managed to sustain a high specific capacity of 144.5 mAh g^{-1} after 900 cycles, corresponding to the capacity retention of 80.3%. Operando synchrotron XRD provides significant structural information during the dynamic K$^+$ intercalation and de-intercalation (Figure 4b). Notably, the operando synchrotron XRD results were collected after 5-cycles activation of the electrodes. Compared with the original V_2C electrode (0.86 nm), the activated V_2C electrode exhibits a much expanded (002) d-spacing of 1.09 nm. Meanwhile, K$^+$ intercalation is accompanied by the appearance of an obvious side peak with d-spacing of 1.15 nm, indicating the structural distortion associated with K$^+$ intercalation. By contrast, the activated ASA-V_2C electrode (1.28 nm) presents only a slight interlayer expansion compared with the original ASA-V_2C electrode (1.25 nm) (Figure 4c). Moreover, the ASA-V_2C electrode demonstrated a zero-strain feature during the K$^+$ intercalation and de-intercalation, with negligible change in the (002) d-spacing. Thereby, we can conclude that the grafted organic molecules effectively buffer the internal stress induced by K$^+$ intercalation, efficiently mitigating the structural distortion of V_2C during repeated charge/discharge cycles.

2.3. Dual-Ion Energy Storage Devices

The high-kinetics K$^+$-storage capability and long-term cycling stability of the ASA-V_2C anode motivated us to explore the assembly of dual-ion energy storage devices (denoted ASA-V_2C//Graphite)

by pairing it with the anion-intercalation graphite cathode. Prior to device assembly, electrochemical performance of the graphite cathode was evaluated using a two-electrode Swagelok cell with the 5 M KFSI electrolyte. The FSI$^-$-intercalation into graphite displayed a high potential window of 3.5 – 5 V versus K$^+$/K with an average discharge potential of 4.4 V versus K$^+$/K (Figure S11a, Supporting Information). The graphite cathode exhibited a decent specific capacity of 100 mAh g^{-1} at 0.05 A g^{-1} and maintained a specific capacity of 75 mAh g^{-1} even at a large current density of 20 A g^{-1}. Moreover, the graphite cathode showed the capacity retention of 89.1% after 200 cycles at a current density of 0.2 A g^{-1} (Figure S11b, Supporting Information). In light of the high ion-intercalation kinetics of both the ASA-V_2C anode and the graphite cathode, we anticipated that the assembled dual-ion devices could deliver simultaneously high energy density and power density.

Considering the specific capacity of the ASA-V_2C anode and the graphite cathode at a low rate, we assembled the dual-ion device with a cathode/anode mass ratio of 1.7. **Figure 5a** illustrates the dual-ion intercalation mechanism of the assembled ASA-V_2C//Graphite device, involving K$^+$ intercalation/de-intercalation of the ASA-V_2C anode and FSI$^-$ intercalation/de-intercalation of the graphite cathode. The CV curve of the ASA-V_2C//Graphite device within 2.5 – 4.5 V at 0.5 mV s^{-1} displays several pairs of redox peaks (Figure 5b), which corresponds to multi-step K$^+$/FSI$^-$ intercalation and de-intercalation processes. To evaluate the rate performance of the device, the GCD measurements were further conducted (Figure 5c). All GCD curves at current densities ranging from 0.1 to 2 A g^{-1} (based on the active materials of both electrodes) show apparent charge/discharge plateaus. Such a dual-ion device is estimated to have a theoretical
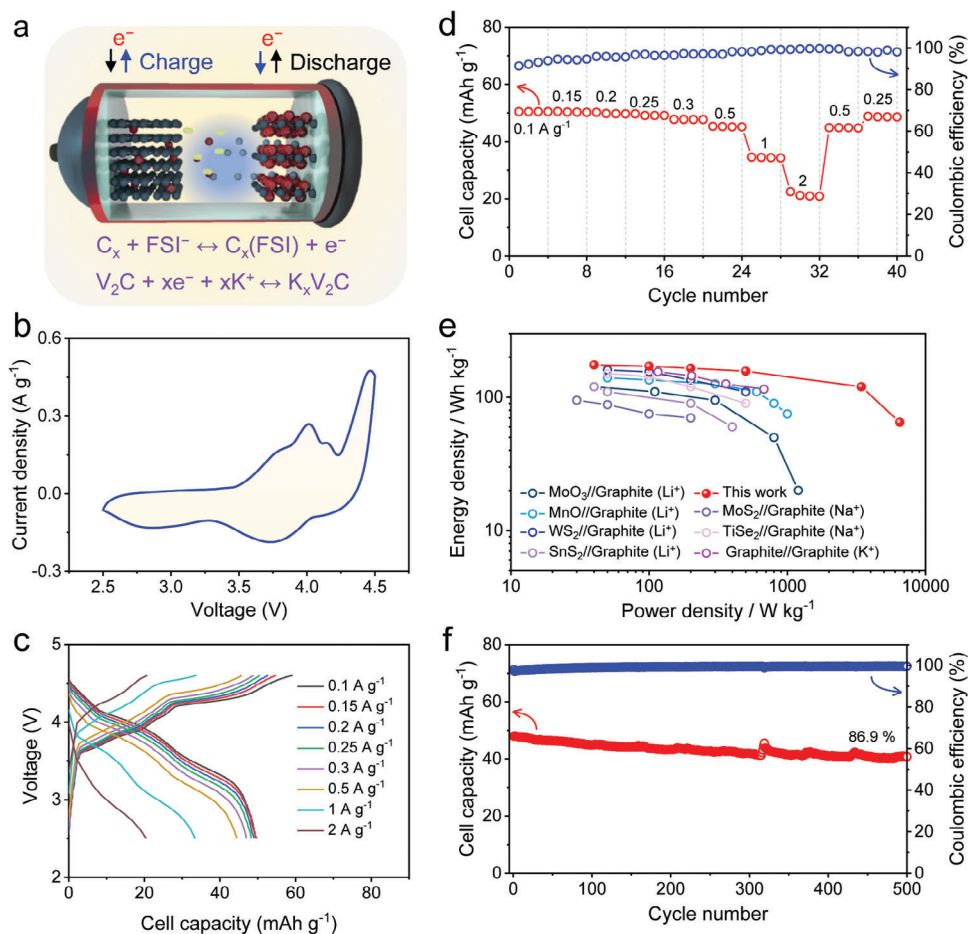
Figure 5. a) Design of the dual-ion intercalation ASA-V$_2$C//Graphite device. On the anode side, K$^+$ is intercalated/de-intercalated between ASA-V$_2$C layers. On the cathode side, graphite is used as a host for FSI$^-$ anion intercalation/de-intercalation. b) CV curve at 0.5 mV s^{-1}, c) GCD profiles at various current densities, and d) rate performance of the ASA-V$_2$C//Graphite device. e) Ragone plots of the ASA-V$_2$C//Graphite device in comparison with reported dual-ion energy storage devices. f) Cycling performance of the ASA-V$_2$C//Graphite device at 0.2 A g^{-1}.

capacity of 64 mAh g^{-1} (based on the active materials of both electrodes). Notably, the assembled ASA-V$_2$C//Graphite device delivered a reversible specific capacity of 51 mAh g^{-1} at 0.1 A g^{-1}, which accounts for 79.6% of its theoretical energy storage capability (Figure 5d). When charged/discharged rapidly at 2 A g^{-1} (37.8 s), the device still achieved a decent specific capacity of 21 mAh g^{-1} with the capacity retention of 41.2%. By comparing the device performance with the half-cell measurements, it becomes evident that the rate capability of the device is predominantly limited by the anion-intercalation kinetics of the graphite cathode.

The energy density and power density of the device were further calculated based on the GCD measurements. Figure 5e presents the Ragone plots of the ASA-V$_2$C//Graphite device in comparison with recently reported dual-ion energy storage devices. Importantly, our device achieved a maximum energy density of 175 Wh kg^{-1}, which is considerably higher than those Li$^+$-based dual-ion devices like SnS$_2$//Graphite (111 Wh kg^{-1}),[45] WS$_2$//Graphite (117 Wh kg^{-1}),[11] MnO//Graphite (137 Wh kg^{-1}),[46] and α-MoO$_3$//Graphite (133 Wh kg^{-1}),[12] Na$^+$-based dual-ion devices, such as TiSe$_2$//Graphite (146 Wh kg^{-1})[13] and MoS$_2$//Graphite (96 Wh kg^{-1})[47] as well as K$^+$-based dual-ion Graphite//Graphite device (155 Wh kg^{-1}).[15] Besides, our

device reached a supercapacitor-comparable power density of 6.5 kW kg^{-1} at an energy density of 65 Wh kg^{-1}.

Lastly, we evaluated the cycling stability of the ASA-V$_2$C//Graphite device at a current density of 0.2 A g^{-1} (Figure 5f). After 500 charge/discharge cycles, the device could maintain 86.9% of its original capacity, which showcases its feasibility for long-term operation. All these results support that ASA-V$_2$C with fast K$^+$-intercalation kinetics can work as a superior anode to construct dual-ion energy storage devices that effectively mitigate the inherent energy-power tradeoff of conventional electrochemical energy storage devices.

3. Conclusion

To summarize, our study has demonstrated the covalent grafting of azobenzene sulfonic acid as an effective approach to remarkably boost the K$^+$-storage kinetics of V$_2$C MXene. The grafted molecule was uncovered to serve multiple functions, including providing the extra K$^+$-storage sites with the equipped azobenzene units, accelerating interlayer K$^+$ diffusion with sulfonate anion as the desirable K$^+$-hopping site, and buffering internal stress induced by K$^+$ intercalation/de-intercalation. These

**ADVANCED
SCIENCE NEWS**

www.advancedsciencenews.com

**ADVANCED
ENERGY
MATERIALS**

www.advenergymat.de

desirable functions collectively resulted in the obtained ASA-V_2C electrode exhibiting significantly boosted K^+-storage capability compared with the pristine V_2C electrode, with considerably enhanced specific capacity (173.9 mAh g^{-1} vs 121.5 mAh g^{-1} at 0.05 A g^{-1}), rate capability (43.1% vs 12.0% at 20 A g^{-1}), and cycling stability (80.3% vs 45.2% after 900 cycles at 0.05 A g^{-1}). Moreover, the ASA-V_2C electrode enabled us to demonstrate a dual-ion energy storage device by coupling it with the FSI^--intercalation graphite cathode, showing a maximum energy density of 175 Wh kg^{-1} and supercapacitor-comparable power density of 6.5 kW kg^{-1}. These encouraging results are expected to inspire the future efforts devoted to tailoring 2D-confined ion storage behaviors, opening new avenues for the development of advanced electrode materials for high-performance energy storage devices.

Supporting Information

Supporting Information is available from the Wiley Online Library or from the author.

Conflict of Interest

The authors declare no conflict of interest.

Data Availability Statement

The data that support the findings of this study are available from the corresponding author upon reasonable request.

[1] M. R. Lukatskaya, B. Dunn, Y. Gogotsi, *Nat. Commun.* **2016**, *7*, 12647.

[2] P. Simon, Y. Gogotsi, *Nat. Mater.* **2020**, *19*, 1151.

[3] D. H. Hathaway, J. A. Eddy, K. Petrovay, J. M. Vaquero, M. C. Gallego, I. G. Usoskin, S. K. Solanki, I. G. Usoskin, B. Kromer, I. G. Usoskin, S. K. Solanki, G. A. Kovaltsov, F. Steinhilber, J. A. Abreu, J. Beer, J. A. Abreu, J. Beer, F. Steinhilber, S. M. Tobias, M. Lockwood, D. V Hoyt, K. H. Schatten, *Science* **2011**, *334*, 1213003.

[4] M. Salanne, B. Rotenberg, K. Naoi, K. Kaneko, P.-L. Taberna, C. P. Grey, B. Dunn, P. Simon, *Nat. Energy* **2016**, *1*, 16070.

[5] Y. Huang, M. Zhu, Y. Huang, Z. Pei, H. Li, Z. Wang, Q. Xue, C. Zhi, *Adv. Mater.* **2016**, *28*, 01928.

[6] Q. Xue, J. Sun, Y. Huang, M. Zhu, Z. Pei, H. Li, Y. Wang, N. Li, H. Zhang, C. Zhi, *Small* **2017**, *13*, 1701827.

[7] Y. Liu, Y. Zhu, Y. Cui, *Nat. Energy* **2019**, *4*, 540.

[8] D. Sabaghi, Z. Wang, P. Bhauriyal, Q. Lu, A. Morag, D. Mikhailovia, P. Hashemi, D. Li, C. Neumann, Z. Liao, A. M. Dominic, A. S. Nia, R. Dong, E. Zschech, A. Turchanin, T. Heine, M. Yu, X. Feng, *Nat. Commun.* **2023**, *14*, 760.

[9] G. Wang, S. Oswald, M. Löffler, K. Müllen, X. Feng, *Adv. Mater.* **2019**, *31*, 1807712.

[10] G. Wang, F. Wang, P. Zhang, J. Zhang, T. Zhang, K. Müllen, X. Feng, *Adv. Mater.* **2018**, *30*, 1802949.

[11] S. Bellani, F. Wang, G. Longoni, L. Najafi, R. Oropesa-Nuñez, A. E. Del Rio Castillo, M. Prato, X. Zhuang, V. Pellegrini, X. Feng, F. Bonaccorso, *Nano Lett.* **2018**, *18*, 7155.

[12] M. Yu, H. Shao, G. Wang, F. Yang, C. Liang, P. Rozier, C.-Z. Wang, X. Lu, P. Simon, X. Feng, *Nat. Commun.* **2020**, *11*, 1348.

[13] R. Zheng, H. Yu, X. Zhang, Y. Ding, M. Xia, K. Cao, J. Shu, A. Vlad, B.-L. Su, *Angew. Chemie – Int. Ed.* **2021**, *60*, 18430.

[14] J. Zhu, Y. Li, B. Yang, L. Liu, J. Li, X. Yan, D. He, *Small* **2018**, *1801836*, 1.

[15] B. Ji, F. Zhang, X. Song, Y. Tang, *Adv. Mater.* **2017**, *29*, 1700519.

[16] K. V. Kravchyk, P. Bhauriyal, L. Piveteau, C. P. Guntlin, B. Pathak, M. V. Kovalenko, *Nat. Commun.* **2018**, *9*, 4469.

[17] W. Zhang, Y. Liu, Z. Guo, *Sci. Adv.* **2019**, *5*, eaav7412.

[18] Y. Li, H. Shao, Z. Lin, J. Lu, L. Liu, B. Duployer, P. O. Å. Persson, P. Eklund, L. Hultman, M. Li, K. Chen, X.-H. Zha, S. Du, P. Rozier, Z. Chai, E. Raymundo-Piñero, P.-L. Taberna, P. Simon, Q. Huang, *Nat. Mater.* **2020**, *19*, 894.

[19] X. Li, Z. Huang, C. E. Shuck, G. Liang, Y. Gogotsi, C. Zhi, *Nat. Rev. Chem.* **2022**, *6*, 389.

[20] H. Wang, J. Li, K. Li, Y. Lin, J. Chen, L. Gao, V. Nicolosi, X. Xiao, J.-M. Lee, *Chem. Soc. Rev.* **2021**, *50*, 1354.

[21] C. (.J.). Zhang, B. Anasori, A. Seral-Ascaso, S.-H. Park, N. Mcevoy, A. Shmeliov, G. S. Duesberg, J. N. Coleman, Y. Gogotsi, V. Nicolosi, *Adv. Mater.* **2017**, *29*, 1702678.

[22] M. R. Lukatskaya, O. Mashtalir, C. E. Ren, Y. Dall'Agnese, P. Rozier, P. L. Taberna, M. Naguib, P. Simon, M. W. Barsoum, Y. Gogotsia, *Science (80-.)* **2023**, *341*, 1241488.

[23] X. Wang, T. S. Mathis, K. Li, Z. Lin, L. Vlcek, T. Torita, N. C. Osti, C. Hatter, P. Urbankowski, A. Sarycheva, M. Tyagi, E. Mamontov, P. Simon, Y. Gogotsi, *Nat. Energy* **2019**, *4*, 241.

[24] C. Zheng, Y. Yao, X. Rui, Y. Feng, D. Yang, H. Pan, Y. Yu, *Adv. Mater.* **2022**, *34*, 2204988

[25] A. Ostadhossein, J. Guo, F. Simeski, M. Ihme, *Commun. Chem.* **2019**, *2*, 95.

[26] B. Sun, Q. Lu, K. Chen, W. Zheng, Z. Liao, N. Lopatik, D. Li, M. Hantusch, S. Zhou, H. I. Wang, Z. Sofer, E. Brunner, E. Zschech, M. Bonn, R. Dronskowski, D. Mikhailova, Q. Liu, D. Zhang, M. Yu, X. Feng, *Adv. Mater.* **2022**, *34*, 2108682.

[27] Z. Sun, J. Zhang, L. Yin, G. Hu, R. Fang, H.-M. Cheng, F. Li, *Nat. Commun.* **2017**, *8*, 14627.

[28] M. Rajapakse, B. Karki, U. O. Abu, S. Pishgar, M. R. K. Musa, S. M. S Riyadh, M. Yu, G. Sumanasekera, J. B. Jasinski, *npj 2D Mater. Appl.* **2021**, *5*, 30.

[29] T. Zhang, L. Chang, X. Zhang, H. Wan, N. Liu, L. Zhou, X. Xiao, *Nat. Commun.* **2022**, *13*, 6731.

[30] M. Naguib, R. A. Adams, Y. Zhao, D. Zemlyanov, A. Varma, J. Nanda, V. G. Pol, *Chem. Commun.* **2017**, *53*, 6883.

[31] C. Eames, M. S Islam, *J. Am. Chem. Soc.* **2014**, *136*, 16270.

[32] Y. Xie, Y. Dall'agnese, M. Naguib, Y. Gogotsi, M. W. Barsoum, H. L. Zhuang, P. R. C. Kent, *ACS Nano* **2014**, *8*, 9606.

[33] F. Ming, H. Liang, W. Zhang, J. Ming, Y. Lei, A.-H. Emwas, H. N. Alshareef, *Nano Energy* **2019**, *62*, 853.

[34] P. Lian, Y. Dong, Z.-S. Wu, S. Zheng, X. Wang, Sen Wang, C. Sun, J. Qin, X. Shi, X. Bao, *Nano Energy* **2017**, *40*, 1.

[35] S. Zhao, Z. Liu, G. Xie, Z. Guo, Z. Guo, F. Song, G. Li, C. Chen, X. Xie, N. Zhang, B. Sun, S. Guo, G. Wang, *Angew. Chem., Int. Ed.* **2021**, *60*, 26246.

[36] F. Ming, H. Liang, G. Huang, Z. Bayhan, H. N. Alshareef, *Adv. Mater.* **2020**, *33*, 2004039.

[37] D. Hetemi, V. Noël, J. Pinson, *Biosensors* **2020**, *10*, 4.

[38] G. Świderski, M. Kalinowska, R. Świsłocka, S. Wojtulewski, W. Lewandowski, *Spectrochim. Acta – Part A Mol. Biomol. Spectrosc.* **2013**, *100*, 41.

[39] Y. Liu, Y. Jiang, Z. Hu, J. Peng, W. Lai, D. Wu, S. Zuo, J. Zhang, B. Chen, Z. Dai, Y. Yang, Y. Huang, W. Zhang, W. Zhao, W. Zhang, L. Wang, S. Chou, *Adv. Funct. Mater.* **2021**, *31*, 2008033.

[40] C. Dicke, M. Morstein, G. Hähner, *Langmuir* **2002**, *18*, 336.

[41] B. L. Hurley, R. L. Mccreery, *J. Electrochem. Soc.* **2004**, *151*, B252.

[42] C. Luo, O. Borodin, X. Ji, S. Hou, K. J. Gaskell, X. Fan, J. Chen, T. Deng, R. Wang, J. Jiang, C. Wang, *Proc. Natl. Acad. Sci. USA* **2005**, *115*, 2004.

[43] F. Mattelaer, K. Geryl, G. Rampelberg, J. Dendooven, C. Detavernier, *ACS Appl. Mater. Interfaces* **2017**, *9*, 13121.

[44] Y. Dong, Z.-S. Wu, S. Zheng, X. Wang, J. Qin, S. Wang, X. Shi, X. Bao, *ACS Nano* **2017**, *11*, 4792.

[45] Y.-B. Fang, W. Zheng, T. Hu, L. Li, W.-H. Yuan, *ACS Omega* **2022**, *7*, 7616.

[46] L.-N. Wu, S.-Y. Shen, Y.-H. Hong, C.-H. Shen, F.-M. Han, F. Fu, X.-D. Zhou, L. Huang, J.-T. Li, S.-G. Sun, *ACS Appl. Mater. Interfaces* **2019**, *11*, 12570.

[47] H. Zhu, F. Zhang, J. Li, Y. Tang, *Small* **2018**, *14*, 1703951.